Contents lists available at ScienceDirect

Chemical Engineering Journal

journal homepage: http://ees.elsevier.com

Effects of Fe^{3+} substitution on Zn-Al layered double hydroxides for enhanced NO photochemical abatement

Adrián Pastor [a], Fredy Rodriguez-Rivas [a,b], Gustavo de Miguel [c], Manuel Cruz-Yusta [a], Francisco Martin [d], Ivana Pavlovic [a,*], Luis Sánchez [a,*]

[a] Departamento de Química Inorgánica, Instituto Universitario de Nanoquímica IUNAN, Universidad de Córdoba, Campus de Rabanales, E-14014 Córdoba, Spain
[b] Departamento de Química, Facultad de Química y Farmacia, Universidad Nacional Autónoma de Honduras (UNAH), Tegucigalpa, Honduras
[c] Departamento de Química Física y Termodinámica Aplicada, Instituto Universitario de Nanoquímica IUNAN, Universidad de Córdoba, Campus de Rabanales, E-14014 Córdoba, Spain
[d] Departamento de Ingeniería Química, Facultad de Ciencias, Universidad de Málaga, Campus de Teatinos, E-29071 Málaga, Spain

ARTICLE INFO

Keywords
LDH
Hydrotalcite
Photocatalyst
Nitrogen oxides

ABSTRACT

In this work the ability of ZnAlFe-CO_3 layered double hydroxides (LDHs) as highly efficient UV–Vis light photocatalysts for the photochemical oxidation of NO gas was studied. LDHs with 3.5 to 4.1 M^{2+}/M^{3+} and 0.33 to 1.55 Fe/Al ratios were prepared by a coprecipitation method. The samples were characterized by different techniques such as XRD, XPS, FT-IR, ICP-MS, TG, SBET, SEM and Diffuse reflectance (DR). The increased presence of the Fe^{3+} ions gave rise to changes in the structure, morphology and optical properties of the LDHs. The prepared ZnAlFe-CO_3 systems exhibited increased surface area and enhanced visible-light absorbance. The photochemical NO abatement resulted in outstanding conversion efficiency (56%) and selectivity (93%) for the iron containing samples, due to a decrease of the e^-/h^+ recombination, higher generation of $^{\bullet}O_2^-$ and $^{\bullet}OH$ radicals and their NO_2 adsorption ability.

1. Introduction

The pollution in urban atmosphere is a major concern for modern society being one of the most serious environmental problems. Among the primary air pollutants, the presence of nitrogen oxides gases (NO_X = NO + NO_2) is highly relevant because they cause several adverse and harmful effects [1]. The transport sector contributes to about 30–40% of the emitted NO_X, of which 80% comes from diesel-powered vehicles [2,3]. As the emissions from diesel cars worsen with age [4], and because of the increase in road traffic, the recommended maximum amount of breathable NO_X is still often exceeded, especially in large cities [5,6].

In recent years, with the aim to confront this environmental problem, photocatalysis has been proposed as a viable technology to remedy NOx pollution (De-NO_X action) at ppb-ppm levels in surrounding air [7]. Thus, photocatalytic De-NO_X removal is carried out in the presence of sunlight, atmospheric oxygen and water, all being abundant and already present in working ambient [8,9]. The feasibility of this remediation technology is demonstrated in many field tests [10,11] and corroborated by a great variety of commercial products available on the market, using TiO_2 as a photocatalyst due to its stable chemical properties. However, the large implementation of this promising air purification technique requires tackling some of the drawbacks observed for TiO_2, such as its inability to exploit the visible light radiation, the low De-NOx selectivity causing emissions of the higher toxic NO_2 molecules in the atmosphere [12–14], and its potential toxicity when inhaled [15]. In this sense, a large variety of semiconductor photocatalysts have been proposed as an alternative to titanium dioxide, with $Cu_{0.08}In_{0.25}ZnS_{1.41}$ [16], $LaFeO_3$-$SrTiO_3$ [17], p-g-C_3N_4 [18], C_3N_4/graphene-$InVO_4$ [19], Bi@$Bi_2O_2SiO_3$ [20], BiOCl [21], $SrCO_3$-BiOI [22], Bi_2MoO_6 [23], Bi/$ZnWO_4$ [24], α-Fe_2O_3 [25], WO_3/ZnO [26], ZnO@SiO_2 [27]; Bi@Bi_2GeO_5 [28], among the latest advanced De-NOx compounds reported.

In this field of research we have just proposed the use of layered double hydroxides (LDH) as promising De-NOx photocatalysts for the first time [29]. LDHs are layered materials with the general formula $[M_{1-x}^{II} M_x^{III}(OH)_2]^{x+} X_{x/n}^{n-} \cdot mH_2O$, where M(II) and M(III) are divalent and trivalent cations and X is the interlayer anion. This structure is similar to that of brucite, $Mg(OH)_2$, where a fraction of M(II) ions is replaced by M(III) ones. The excess of positive charge in the layers is balanced by intercalating anions and water molecules in the interlayer space. Metal ions and interlayer anions may vary over a wide range, while a metal ratio M(II)/M(III) could be in the range $0.1 < x < 0.33$ [30]. Recently, LDHs were considered as novel photocatalysts

* Corresponding authors.
E-mail addresses: pauli@uco.es (I. Pavlovic); luis-sanchez@uco.es (L. Sánchez)

https://doi.org/10.1016/j.cej.2020.124110
Received 25 September 2019; Received in revised form 19 December 2019; Accepted 11 January 2020
Available online xxx
1385-8947/

in processes such as aerobic degradation of pollutants [31], photocatalytic water splitting [32] and CO_2 photoreduction [33]. The unique structure, uniform distribution of different metal cations in the brucite layer, surface hydroxyl groups, flexible tunability, a variety of intercalated anions in their interlayer spaces, swelling properties, oxo-bridged linkage, high chemical stability and easy preparation are some of the encouraging advantages of the use of this group of materials as photocatalysts [34].

In the field of De-NOx photochemical processing, and considering the high efficiency and selectivity of a Zn based photocatalyst [26,27], our first approach in the use of LDH was related to the ZnAl-CO_3 system [29]. This photocatalyst, working under UV light, exhibited high NO removal efficiencies and impressive selectivity to the De-NOx process. However new advances are necessary in the search of photocatalysts to be used in applications for DeNOx remediation of urban atmosphere, where the availability of UV light is sometimes limited due to the urban architecture, geographical location and gloomy weather conditions [7]. Thus, the visible light activation of a DeNOx photocatalyst is mandatory. To this aim, the present work treats the effect that gradual Fe^{3+} for Al^{3+} replacement has on improving LDH De-NOx performance, i.e. on shifting their photocatalytic activity to the visible range and the enhanced NO_2 adsorption. Moreover, by using EPR and PL techniques, the enhanced photocatalytic mechanism of NO_X removal by using ZnAlFe-CO_3 LDH was explained.

2. Materials and methods

$Zn(NO_3)_2{\cdot}6H_2O$, $Al(NO_3){\cdot}9H_2O$ and $Fe(NO_3){\cdot}9H_2O$ were purchased from PanReac AppliChem. 5,5-dimethyl-l-pyrroline-N-oxide (DMPO) was acquired from Sigma Aldrich. All the chemicals were at least 98–99% pure and demineralized water was used in the experimental section.

2.1. Synthesis of LDHs

The coprecipitation method was used to synthetize ZnAlFe-LDHs with different Fe/Al ratios. 100 mL of 0.015 M solution of $Zn(NO_3)_2{\cdot}6H_2O$, $Al(NO_3){\cdot}9H_2O$ and $Fe(NO_3){\cdot}9H_2O$ (Zn/(Fe + Al) = 4; Fe/Al = 0, 0.3, 0.6, 0.9, 1.2, 1.5) was added drop-wise into 100 mL of 0.01 M Na_2CO_3 solution under stirring at room temperature. The constant pH = 10 was kept by dropping a 2.0 M NaOH solution during the coprecipitation reaction. The slurry obtained was then stirred for 3 h, centrifuged, washed with distilled water to be neutral (pH = 7.0), and dried in an oven at 60 °C. The LDHs prepared were labeled as ZAF0, ZAF0.3, ZAF0.6, ZAF0.9, ZAF1.2 and ZAF1.5, the number denoting the initial Fe/Al ratio.

2.2. Characterization of the photocatalysts

X-ray diffraction (XRD) patterns of powdered samples were collected on a Bruker D8 Discovery instrument using Cu Kα radiation (λ = 1.5405 Å) at the step size and step counting time of 0.02° (2θ) and 0.65 s, respectively. Infrared spectra (IR) analyses from 450 to 4000 cm^{-1} were carried out on transmission mode in a FT-MIR Bruker Tensor 27 with a resolution of 1 cm^{-1}. Nitrogen adsorption–desorption isotherms were recorded at 77.4 k in an ASAP 2020 apparatus (Micromeritics). Prior to the sorption measurements, samples were degassed at 105 °C under vacuum for 3 h. Specific surface areas were estimated from the N_2 adsorption isotherms, using the multipoint Brunauer–Emmett–Teller (BET) method over the relative equilibrium pressure interval $0.05 < P/P_0 < 0.30$. Scanning electron microscopy (SEM) images were obtained with a Helios Nanolab 650 microscope. Analyses of chemical compositions of LDHs were performed with induced coupled plasma mass spectroscopy (ICP-MS; Perkin Elmer Nexion X) after dissolving the samples in 0.1 M HCl. The water content of LDH was calculated from the thermogravimetric (TG) analysis which was obtained by using a Mettler Toledo apparatus in air atmosphere (flow: 100 mL min^{-1}) at a heating rate of 10 °C min^{-1}.

Diffuse reflectance (DR) spectra were collected from 200 to 800 nm in a Varian Cary 1E spectrophotometer, at a rate of 30 nm min^{-1} and a step of 0.5 nm. X-ray photoelectron spectra (XPS) were recorded using non-monochromated MgK radiation (hν = 1253.6 eV) and a hemi-spherical analyser operating at a constant pass energy of 29.35 eV (Physical Electronics PHI 5700 spectrometer): The X-ray generator operated at 15 kV and 300 W. The pressure in the analysis chamber was about 10^{-7} Pa. Binding energies were corrected against those for C 1 s peak of adventitious carbon fixed at 284.8 eV. The XPS peaks were curve-fitted by the software MultiPak version 9.3 using a convolution of independent Gaussian and Lorentzian contributions (the so-called Voigt profile). The steady-state photoluminescence (PL) emission spectra were collected on a FLS920 Fluorimeter (Edinburgh Instrument Ltd, Livingston, UK). Electron paramagnetic resonance (EPR) spectra were recorded in an EMXmicro (Bruker) spectrometer at room temperature. LDH powder was dispersed in a solution (water or methanol for detecting •OH or $\bullet O_2^-$, respectively) with 45 mM DMPO as the spin-trap agent and irradiated for 15 min with artificial sunlight (Xe Lamp).

2.3. Photocatalytic activity evaluation

The experimental conditions to carry out the photocatalytic tests, were based on ISO 22197-1, a method used to characterize the air purification measurement. The performance of LDHs in photo-oxidizing NO gas was assessed in a laminar flow reactor which contained a 50 × 50 mm sample holder. The reactor was placed inside a light sealed irradiation box (Solarbox 3000e RH) equipped with a Xe lamp with controlled irradiance. LDHs were irradiated with artificial sunlight (irradiances of 25 and 580 Wm^{-2} for UV and visible light) using 500 mg of sample powder in each test. Synthetic air and pure NO were mixed to create a simulated polluted urban atmosphere of 150 ppb [35] and sent to the reactor (flow rate gas = 0.30 l min^{-1}). Air was previously passed through a gas-washing bottle filled with demineralized water in order to maintain the relative humidity at 50 ± 5%. The concentration of NO, NO_X and NO_2 gases from the reactor was continuously measured in a chemiluminescence analyzer (model Environment AC32M). Before and after the irradiation period of each test, the air/NO gas mixture was passed over the sample in the dark for 15 min to discard the existence of NO_X adsorption. Besides, there was no NO photolysis when the photocatalytic test was carried out in the absence of the sample. Each test was done three times in order to calculate the average concentration values. The calculated standard deviations were ± 0.3 ppb for NO concentration and ± 1.0 ppb for NO_2 and NO_X concentrations. The photocatalytic activity of the samples was studied regarding the following facets:

$$NO\ conversion(\%) = \frac{([NO]_{in} - [NO]_{out})}{[NO]_{in}} \times 100 \quad (1)$$

$$NOx\ conversion(\%) = \frac{([NOx]_{in} - [NOx]_{out})}{[NOx]_{in}} \times 100 \quad (2)$$

$$\text{Selectivity; } S\ (\%) = \frac{([NOx]_{in} - [NOx]_{out})/[NOx]_{in}}{([NO]_{in} - [NO]_{out})/[NO]_{in}} \times 100 \quad (3)$$

where $[NO]_{in}$, $[NO_X]_{in}$ and $[NO]_{out}$, $[NO_X]_{out}$ represent the measured inlet and outlet concentrations, respectively, and $[NO_X] = [NO] + [NO_2]$.

3. Results and discussion

3.1. Phase and composition

The XRD patterns corresponding to the ZnAl-LDH and ZnAlFe-LDH samples are shown in Fig. 1. All the recorded XRD patterns are characteristic of layered double hydroxides, with higher intensity peaks (a basal diffraction plane with its corresponding harmonics, *0 0 l*) at 2Θ values below 30°, and with broader and lower intensity (*h k l*) peaks above this value [36]. The basal spacing of around d_{003} = 7.6 Å obtained for all samples indicates that the carbonate anion is situated in the interlayer of LDH [37]. In comparison with the ZnAl-CO_3 LDH system previously reported [29], the XRD reflection peaks in the ZnAlFe-LDH samples are small and broad, suggesting that gradual substitution of Al^{3+} by Fe^{3+} provokes a decrease in the size of the crystalline domains of the samples. XRD patterns also show that the replacement of Al^{3+} for Fe^{3+} ions in the samples provokes a slight shift of the *0 0 l* reflections towards higher two theta degrees, thus indicating that the value of the lattice parameter *c* decreases (Table S1). This presence of Fe^{3+} increases the effective layer charge and thus increases the attraction between positive layers and interlayer anions. Moreover, the slightly larger ionic radius of Fe^{3+} (0.69 Å) with respect to Al^{3+} (0.67 Å) causes a slight increase in the lattice parameter *a*.

In Fig. 1, it is observed that XRD patterns of the ZnAlFe-LDH samples are similar in the 0.33–1.22 Fe/Al ratio range, confirming the crystallization of only a pure LDH phase. However, when increasing this ratio to 1.55 significant changes are observed in the XRD pattern of the ZAF1.5 sample (Fig. 1). Now a new low intensity reflection appears at around 17 two-tetha degrees and the (0 1 2) plane becomes higher in intensity and slightly shifts two-theta degrees higher. Both reflections could be tentatively assigned to the presence of the $Fe_2CO_3(OH)_2$ phase (ICDD card n° 01-076-6357) [38]. Figure S1 (in Supplementary Information) comparatively shows the C 1s, O 1s, Fe 2p, and Zn LMM normalized XPS spectra of the ZAF1.2 and ZAF1.5 samples. In addition to the peak of adventitious C (284.8 eV), the intensity of the peak at 289 eV associated with CO_3^{2-}(OH$^-$) [39] is higher for the sample ZAF1.5, which corroborates that by XRD. All the rest of the samples showed a peak at 289 eV with an intensity similar to that shown for sample ZAF1.2 (Fig. S1). O1s peak at 531.4 eV was attributed to CO_3^{2-} and OH$^-$ [39–41]. Figure S1 also shows the pattern of the Zn LMM Auger bands, with the main peak at around 988 eV kinetic energy (498 eV binding energy) corresponding to the $Zn_5(CO_3^{2-})_2(OH^-)_6$ [39]. As shown by the pattern of the Al 2p (not shown) and Fe 3p regions and their binding energies (Fig. S1), the oxidation states were Al^{3+} and Fe^{3+}, respectively.

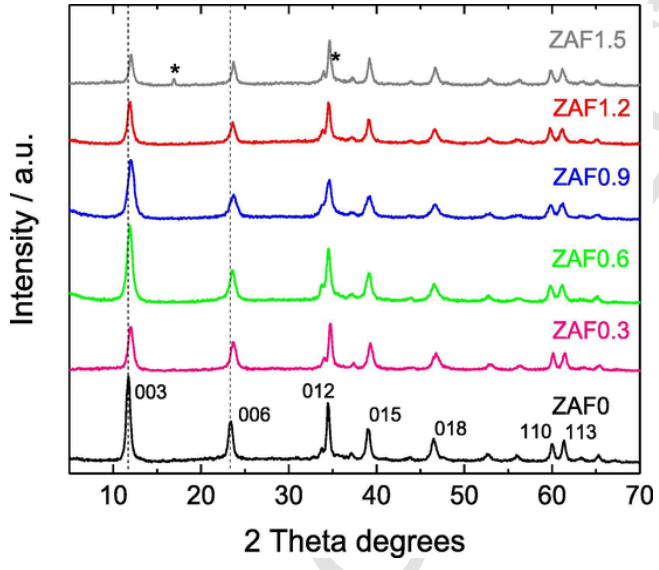

Fig. 1. XRD patterns for the ZnAl-LDH and ZnAlFe-LDH samples (*: $Fe_2CO_3(OH)_2$).

The Fourier Transform Infrared (FT-IR) spectra of the samples ZAF0 and ZAF0.6, by way of example, is included in Fig. S2 and is characteristic of LDH compounds [36]. The most representative features are: a broad band around 3500 cm^{-1} corresponding to the hydroxyl groups vibrations, a band at 1634 cm^{-1} due to the bending mode of water molecules and the splited band around 1400 cm^{-1} (at 1366 cm^{-1} and 1507 cm^{-1}) of the carbonate ν_3 antisymmetric vibration mode. This splitting is a consequence of the symmetry lowering from D_{3h} to C_{2v}, for the free carbonate and the interlayered LDH carbonate, respectively, due to its interaction with the OH$^-$ groups and H_2O molecules. This splitting is more pronounced for ZnAlFe LDH phases [36] which confirms the Fe presence in LDH brucite-layers (Fig. S2). The decrease of symmetry, also gives rise to the activation of carbonate ν_1 mode, infrared inactive in the free carbonate, with the corresponding band around 1075 cm^{-1}, together with the bending vibrations of OH groups in the 850–1000 cm^{-1} range. However, this range of IR spectrum is more complex because the carbonate bands could be overlapped with OH groups and metal–oxygen vibrational bands, as is the case in the ZAF sample [36,42,43].

Table 1 shows the data corresponding to the chemical analysis of the pure LDH samples. In the case of the ZAF0, the Zn/Al molar ratio is similar to that of the starting solution used to prepare the LDH material. However, as the amount of iron increases, the Zn^{2+}/M^{3+} molar ratio decreases, indicating the difficulty to preserve the M^{2+}/M^{3+} ratio constant during the building of the LDH framework. The Zn/(Al + Fe) atomic ratio, together with the number of water molecules (those calculated from the first weight loss in the TG curve), were used to propose the chemical formulae of the samples. It was assumed that the carbonate anions compensate all positive charge caused by the presence of M^{3+} ions in the layers.

3.2. Morphology and porous structure of photocatalysts

The method of synthesis here used involves obtaining poorly crystalline samples. Thus for the ZAF0 sample, without iron, the typical hexagonal sheet-like structure expected for ZnAl-CO_3 LDHs was not completely formed, and the particles appear as rounded pseudo-hexag-

Table 1
Chemical and physical properties for the pure LDH samples: metal content and ratio; proposed formulae; BET surface and band gap energy value.

Sample	% Atomic			Atomic ratio		Proposed Formula	S_{BET}	Band gap (eV)
	Zn	Al	Fe	Zn/Al + Fe	Fe/Al		($m^2 g^{-1}$)	
ZAF0	63.16	15.34	–	4.11	–	$[Zn_{0.81}Al_{0.19}(OH)_2](CO_3)_{0.1}\cdot 0.67H_2O$	57.9	3.52
ZAF0.3	63.62	12.49	3.9	3.88	0.31	$[Zn_{0.80}Al_{0.15}Fe_{0.05}(OH)_2](CO_3)_{0.1}\cdot 0.48H_2O$	63.5	3.21
ZAF0.6	63.62	10.30	6.51	3.78	0.63	$[Zn_{0.79}Al_{0.13}Fe_{0.08}(OH)_2](CO_3)_{0.11}\cdot 0.50H_2O$	72.6	3.13
ZAF0.9	61.02	8.96	8.34	3.53	0.93	$[Zn_{0.78}Al_{0.11}Fe_{0.10}(OH)_2](CO_3)_{0.11}\cdot 0.62H_2O$	79.3	2.84
ZAF1.2	62.25	7.74	9.47	3.61	1.22	$[Zn_{0.78}Al_{0.10}Fe_{0.12}(OH)_2](CO_3)_{0.11}\cdot 0.68H_2O$	87.8	2.62

onal sheets, as observed in the SEM images shown in Fig. 2. The crystallization becomes poorer with the presence and increase of the amount of iron in the chemical formulae, the sheets being mixed with aggregates of smaller amorphous particles. In the same way, the presence of iron seems to restrain the pillaring of LDH. In fact, the thickness of the platelets clearly decreases from 34 nm for the ZAF0 to 13 nm observed for the ZAF0.9 and ZAF1.2 samples, Fig. S3.

Subsequently, the surface area and porous structure were elucidated from the corresponding N_2 adsorption-desorption isotherm of the different samples, Fig. 3. The isotherm shape which corresponds to a type II, according to IUPAC classification [44] and characteristic of the adsorption on macro and non-porous materials, is similar to that reported for ZnAl LDHs [29,45]. At high relative pressure, $P/P_0 > 0.85$, the isotherms exhibit a H1 hysteresis loop, suggesting the presence of mesopores. The H1 loop is characteristic of agglomerates arranged in a fairly uniform way, indicating relatively high pore size uniformity and facile pore connectivity [45]. In fact, a slight broadening of the hysteresis loop occurs when the amount of Fe in the LDH samples is increased, in agreement with the non-uniform particle size distribution observed by SEM. Specific surface areas determined by BET method are given in Table 1 and were higher for Fe substituted samples, increasing with the iron content, which is in agreement with their lower cristallinity, as was confirmed by XRD (Fig. 1) and SEM characterization (Fig. 2).

3.3. Optical properties

The corresponding UV–Vis spectra of the samples are shown in Fig. 4a. The absorption spectrum obtained for the ZAF0 sample is as expected for Zn-Al LHDs [46,47]. As Al^{3+} ions are replaced by Fe^{3+}, the absorbance increases and new bands characteristics of Zn-Fe LDHs appear at 280, 414 and 480 nm, assigned to ligand-to-metal charge transfer (O → Fe) for Fe^{3+} species octahedrally coordinated within the brucite-like sheets [48–51]. The incorporation of iron ions in the LDH structure results in the enhancement of the visible light absorption, in agreement with the appearance of a reddish colour in the samples (Fig. S4).

The acquired diffused reflectance spectra were converted to the Kubelka–Munk function $[F(R_\infty)h\nu]^2$ with the objective to determine the value of the optical band gap (E_g). The band gap energies of the samples are estimated from the tangent lines in the plots of the modified Kubelka–Munk function vs. the energy of exciting light [47], as shown in Fig. 4b. The calculated band-gap energy for the ZAF0 was 3.52 eV (Table 1), this value decreasing as the iron content increased in the LDH compound. Thus for the ZAF1.2 sample, those with the

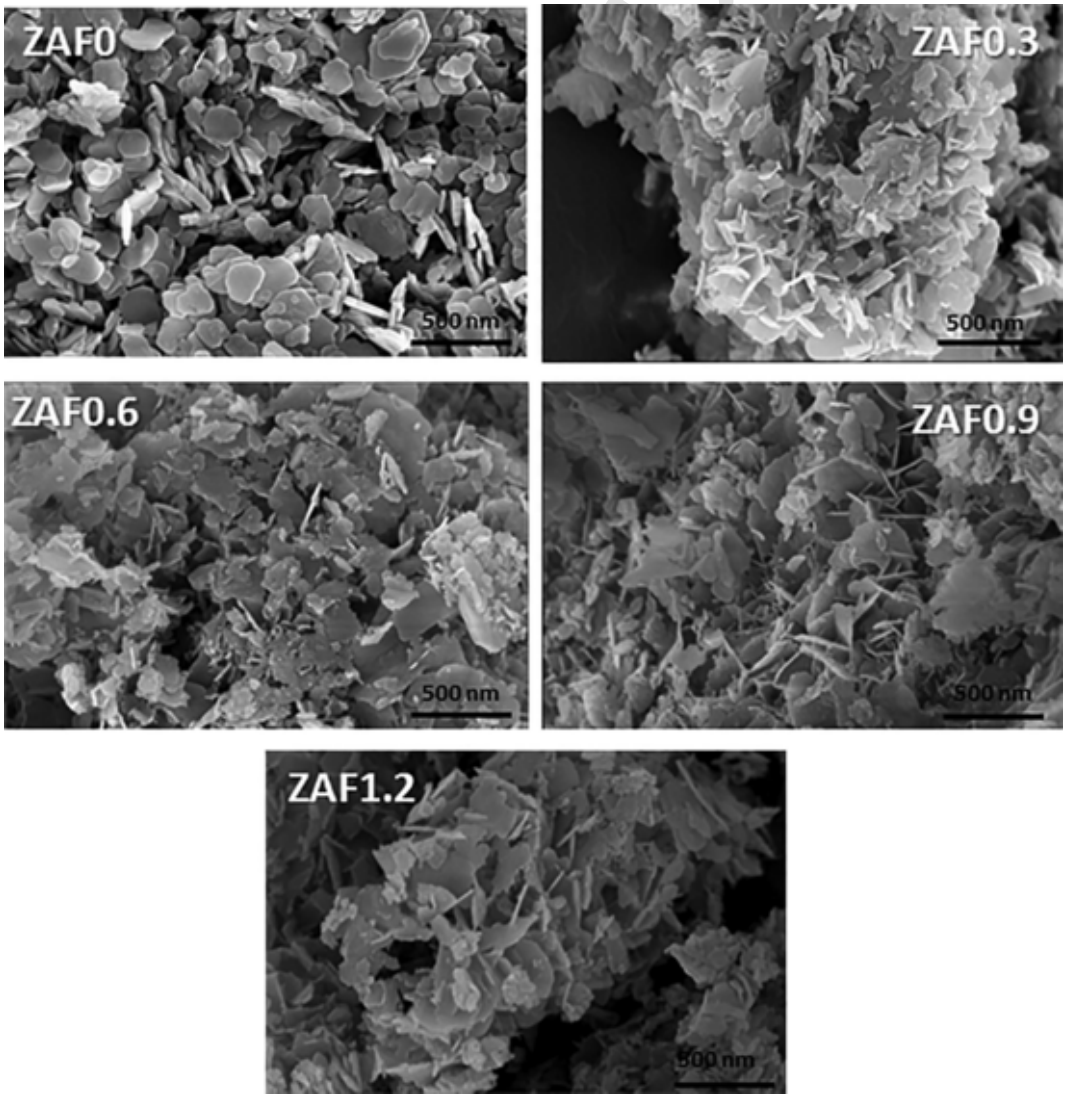

Fig. 2. SEM images for the ZnAl-LDH and ZnAlFe-LDH samples.

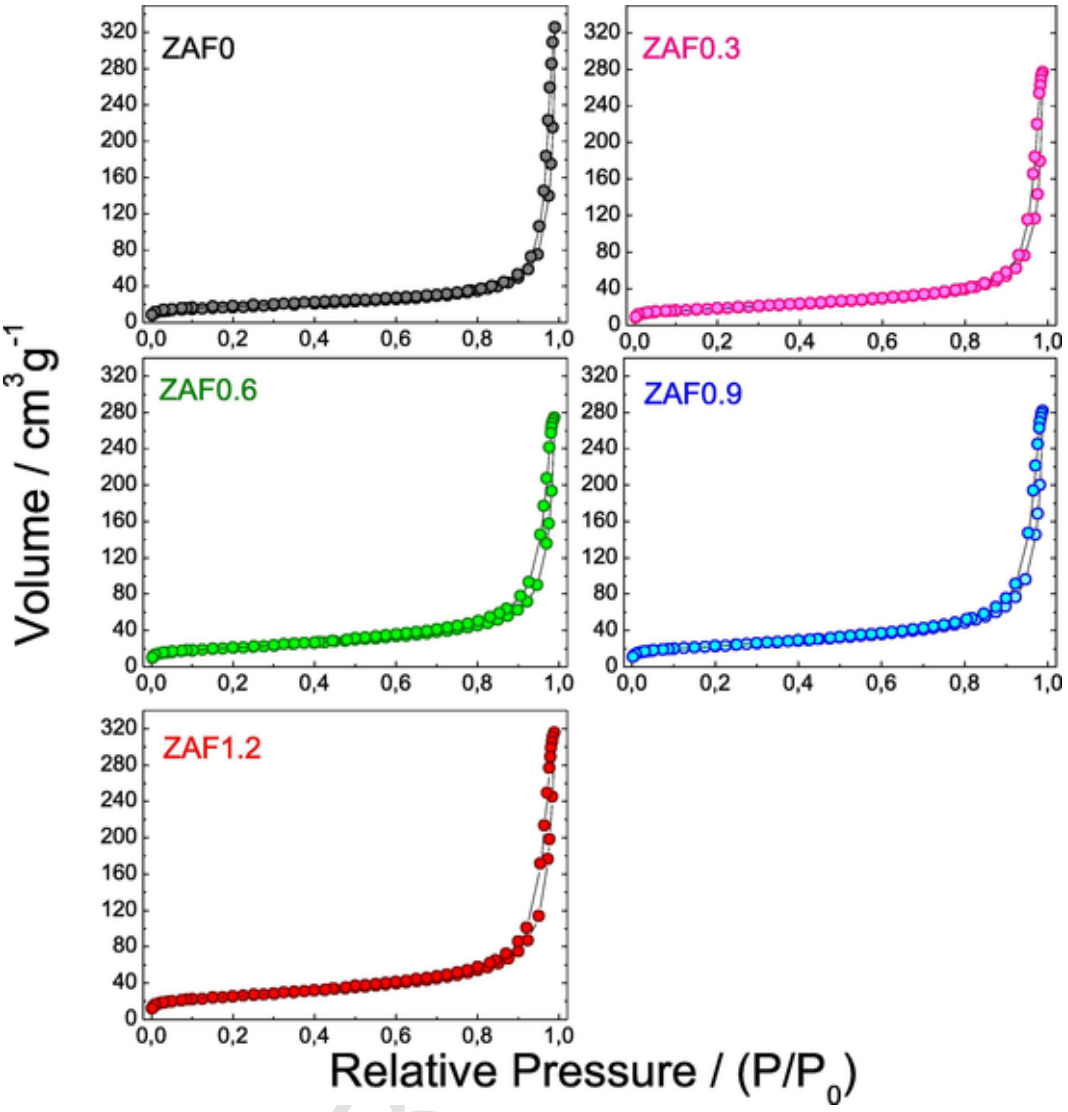

Fig. 3. N_2 adsorption-desorption isotherms for the ZnAl-LDH and ZnAlFe-LDH samples.

higher content in Fe, a value of 2.62 eV is measured, similar to that previously reported for Zn-Fe LDHs materials [37,39].

3.4. Photocatalytic NO removal

The photochemical abatement of NO gas using ZnAlFe-LDH photocatalysts was studied. As previously reported by our group, ZnAl-LDHs are able to activate the complete oxidation of NO molecules to nitrate species under sunlight irradiation [29]. Thus, once the LDH particles absorb light, an electron transfer from the valence band (VB) to the conduction band (CB) occurs. The pairs of mobile charges (e^- and h^+) reaching the surface of the semiconductor particles [45,49] produce, as we will discuss later, reactive oxygen species (ROS) from the adsorbed water molecules, initiating the progressive oxidation of NO gas [7,25,52,53]. The occurrence of this NO photochemical removal process is simply confirmed through the observation of the evolution of the nitrogen oxide gases concentration recorded for the ZnAl-LDH and ZnAlFe-LDH samples as a function of sunlight irradiation time, Fig. 5a. In the absence of light for the first 15 min, the inlet NO concentration remained constant indicating no physico-chemical interaction with the photocatalyst. However, a sudden decrease of NO concentration occurred just when the lamp was turned on. Under light irradiation, the NO removal rapidly increased on time (60 min) and reached a constant value, indicating the achievement of a stable photo-oxidation activity. The photochemical process stopped when illumination was shut down. Interesting differences were found for the NO abatement ability measured in the ZnAl-LDH and ZnAlFe-LDH samples. The presence of Fe in the LDH compound enhanced the NO abatement in 4–11%. The increased efficiency observed for the enriched iron samples is related with their higher surface area, which facilitates the contact between the reactant molecules and the metallic photo-active centres. Morevover, the amount of Fe^{3+} present in the LDH sample is highly relevant to the photochemical activity measured under only visible light ($\lambda > 510$ nm), Fig. 5b, in correlation with the changes in the band gap values measured (Table 1). Subsequently, a minor amount of NO molecules (10–17 ppbs) are removed from the reaction chamber, which is reasonable considering that the presence of Fe is 7 to 15 times lower than that of Zn in the LDH formulae. Interestingly, in spite of the minor presence of Fe, the efficiency in the NO abatement clearly increases with the content of iron. This is indicative that, under visible light, the iron centres are responsible for the light absorption and the photochemical oxidation process. In fact, in the absence of iron (ZAF0 sample), the NO abatement was not detected (Fig. 5b). Therefore,

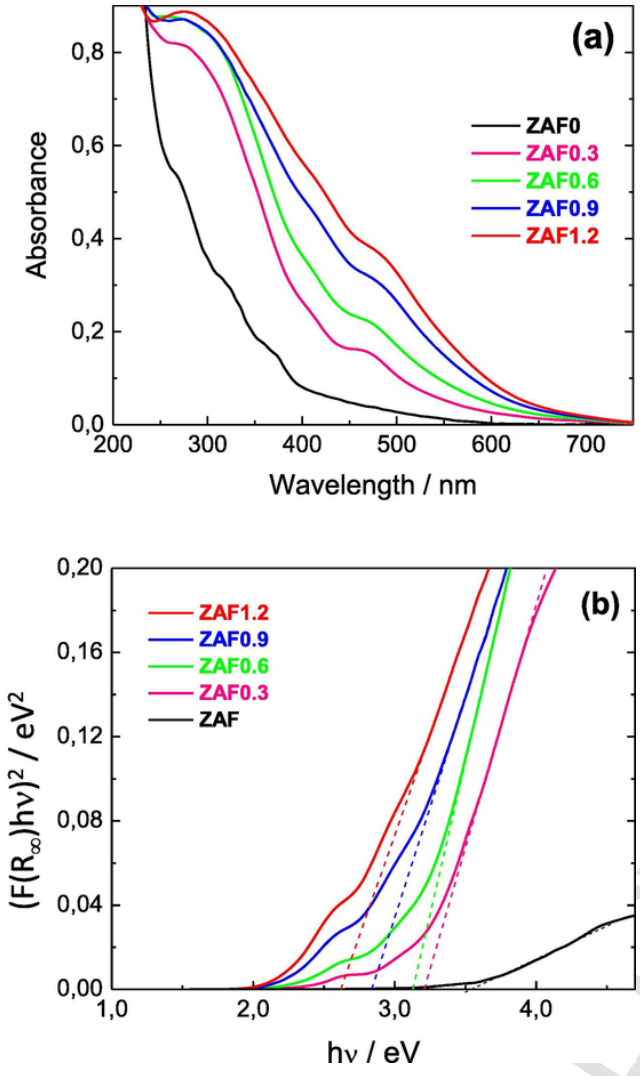

Fig. 4. The UV–Vis absorption spectra (a) and the Kubelka-Munk transformed reflectance spectra (b) for ZnAl-LDH and ZnAlFe-LDH samples.

the replacement of Al^{3+} by Fe^{3+} ions converts the LDH into a De-NOx visible light photocatalyst.

Apart from the enhanced NO removal, the ZnAlFe-LDH samples are of interest because of their higher De-NOx selectivity values. During the NO photochemical oxidation, the NO_2 gas appears as an intermediate, undesired specie because it is much more dangerous than NO [12]. The De-NOx selectivity term [54], *S*, defines the ratio of degraded NO that is ultimately converted into harmless nitrate rather than into toxic nitrogen dioxide. In Fig. 5c, it can be observed that the amount of NO_2 raised molecules when using ZnAlFe-LDH photocatalysts, is nearly half that obtained by using ZnAl-LDH. As previously reported by our group [29], in similarity to ZnO systems [27,55], the ZnAl-LDH exhibits outstanding De-NOx selectivity due to the sensitivity to NO_2 gas. Thus, the preliminary NO_2 adsorption studies carried out on the ZAF0 and ZAF0.3 samples in the dark, Fig. S5, show that lower concentration values for NO_2 are measured during the first 30 min, in comparison to that of a blank test (without the presence of a catalyst) in which the gas concentration remained constant. This is indicative that, during the De-NOx process, the NO_2 gas molecules are probably being adsorbed on the surface of LDHs, facilitating their oxidation to nitrate before being released into the atmosphere. In Fig. S5, both samples ZAF0 and ZAF0.3 exhibited a similar NO_2 gas adsorption profile in agreement with their similar values of Zn content and specific surface area. How-

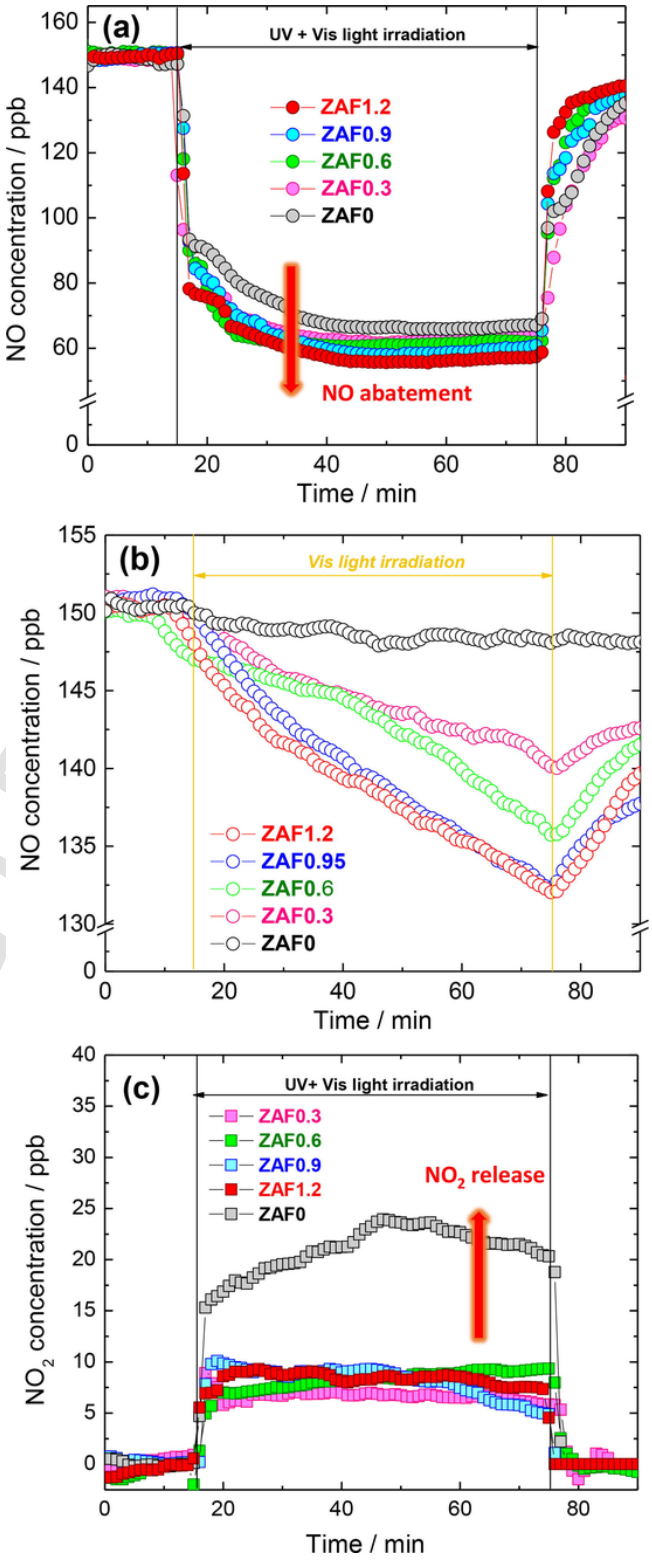

Fig. 5. Nitrogen oxides concentration profiles obtained during the photo-degradation of gaseous NO under light irradiation on the ZnAl-LDH and ZnAlFe-LDH samples.

ever, the release of NO_2 is doubled when the De-NOx reaction is performed with the ZAF0 sample, Fig. 5c. This would be indicative that physical as well as electronic govern the photochemical oxidation, as discussed below.

For practical considerations, Fig. 6a shows the NO and NO_X conversion and the *S* values measured from De-NO_X tests performed on photo-

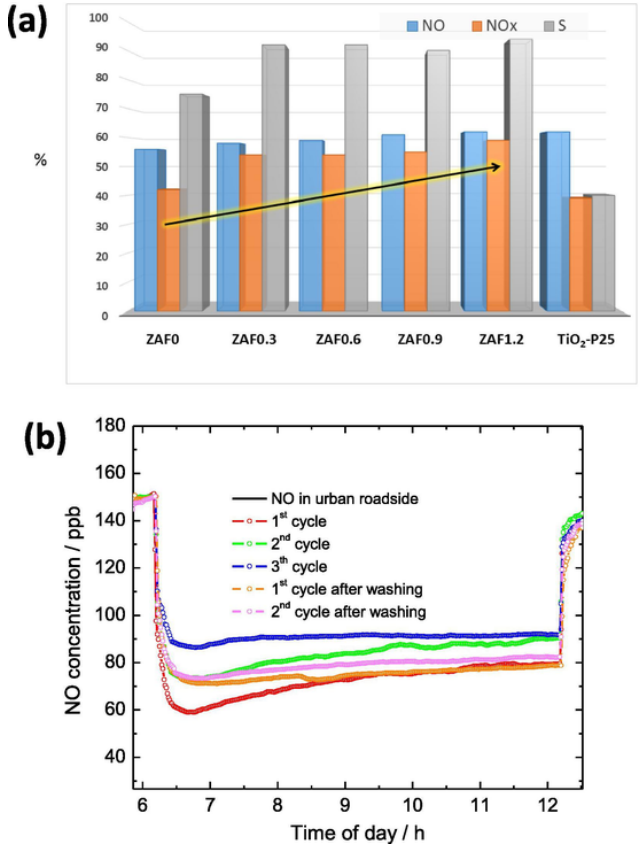

Fig. 6. (a) NO conversion, NO_X conversion and Selectivity values (%) for the ZnAl-LDH, ZnAlFe-LDH and TiO_2-P25 samples. (b) The diurnal distribution pattern of NO gas at urban roadsides and the NO concentration profile obtained for the ZAF1.2 sample (o) at different runs during 6 h of light irradiation. The sample was washed and dried after the 3rd run.

tacalysts and compared with those for Aeroxide® TiO_2 P25 (Evonik), a material broadly used worldwide as a reference in photocatalytic De-NO_X processes. The photocatalyst reusability is represented in Fig. 6b. Due to their excellent S values around 92%, the ZnAlFe-LDH photocatalysts possess a higher ability to remove the NOx oxides with an efficiency of about 30%, higher than that of the non-substituted ZnAl-LDH. These values are in line with the NO conversion (45–70%) and selectivity (84–98%) values recently reported for De-NOx photocatalysts [13,21,23,27,56–58]. The measured values stand out from that of the TiO_2 P25 benchmark product, obtained under identical experimental conditions. As inferred from the nitrogen oxides concentration profiles obtained during the photo-degradation of gaseous NO on TiO_2 P25, Fig. S6a, this photocatalyst exhibited poor ability to avoid the release of NO_2 gas during the photochemical test [59]. The TiO_2 P25 did not show sensitivity to adsorb NO_2 gas [27], which would imply that the newly formed NO_2 molecules are released into the atmosphere before being oxidized. Therefore, its low De-NOx selectivity (40%) is detrimental for favourable NOx removal efficiency. Moreover, no photochemical activity was measured for TiO_2 P25 under visible light irradiation, Fig. S6b. Fig. 6b shows the diurnal mean values of NO concentration, reaching its maximum level (≈180 ppb) between 6.00 and 12.00 in the morning, measured at an urban roadside in a highly populated city [35]. It is of interest to know how the ZnAlFe-LDH could serve to abate this main NO_X peak concentration level. Thus, the ZAF1.2 sample was subjected to three consecutive NO photocatalytic removal experiments run in periods of 6 h under similar NO concentrations (NO inlet concentration of 150 ppb). The data collected (Fig. 6b) suggest that half of the pollution peak is abated, decreasing the photocatalytic efficiency by around 6% in the first three cycles due to the deposition of the nitrite/nitrate species during the photochemical oxidation process [27,29]. With the aim of eliminating these species, the sample was washed with milli-Q water (filtered, collected and dried) after the third run. Subsequently, the efficiency was recovered in the next two runs (1st and 2nd after washing) indicating good regeneration and reusability for this type of photocatalyst. Therefore, the ZnAlFe-LDH can be considered as a useful photocatalyst in the abatement of the NO urban pollution.

3.5. Charge separation and oxidation mechanism

Recently, our research group reported on the ability of ZnAl-LDH to photochemically remove the NO_X from air by its conversion into nitrate ions [29]. In the presence of oxygen and water molecules, the photocatalytic oxidation mechanism is briefly summarized in the $NO \rightarrow HNO_2 \rightarrow NO_2 \rightarrow NO_3^-$ sequential steps [29], assisting the reactive oxygen species (ROS), hydroxyl and/or superoxide radicals, as strong oxidants. The efficiency and active species involved in this mechanism when using the ZnAlFe-LDH photocatalyst are studied.

Photoluminescence (PL) spectroscopy is commonly used to study the photocharge generation, transfer and separation efficiency of photocatalysts, including LDH compounds [60]. Fig. 7a shows the PL signal corresponding to the ZnAl-LDH [61] and ZnAlFe-LDH photocatalysts. Under appropriate light illumination, the electrons in the valence band of ZnAl-LDH are promoted to the conduction band, leaving a hole in the valence band. The electrons in the conduction band are taken up by the Al atoms while the surface OH groups accept the photogenerated holes, which minimizes the e^-/h^+ recombination. These photogenerated charges initiate the formation of radical reactive species [62–64]. The high PL intensity measured for the non-substituted ZnAl-LDH is indicative of the high radiative recombination rate of the electrons and holes in the semiconductor, which competes with the reaction of the photogenerated charges with oxygen and water molecules to form the reactive oxygen species [19]. However, the PL signal is strongly attenuated by the presence of the iron centres in all the ZnAlFe-LDH samples. This behaviour clearly indicates that a new deactivation pathway for the photocharges is now available due to the presence of the iron centres. It is well-known that iron doping introduces energy levels into the band gap of the ZnAl-LDH semiconductor which may act as electron scavengers [46]. Moreover, the MMCT (metal to metal charge transfer) electron transition through the oxo-bridged binuclear M^{III}–O–M^{II} linkages constructed in LDHs has been previously reported for catalysts absorbing visible light [64–66]. In a similar way, the absence of any PL signal in the ZnAlFe-LDH samples could reveal that the photogenerated charge is mainly transferred from the zinc to the iron centres even at low percentages of this metal. The MMCT electron transition will result in the production of superoxide anion radical, which is one of the main oxidative species in the $NO \rightarrow NO_3^-$ process. This effect should produce an enhancement of the catalytic reaction rates, which is in agreement with the enhanced performance commented above.

On the other hand, to shed light on the reactive species evolved in the photochemical reaction over the ZnAl-LDH and ZnAlFe-LDH samples, EPR measurements were conducted using DMPO as the spin-trapping agent under sunlight excitation, Fig. 7b and c. No signal was detected when the photocatalyst suspension was in the dark. The strong characteristic signals of $^{\bullet}O_2^-$ were detected in a methanolic dispersion of the ZnAl-LDH and ZnAlFe-LDH samples (Fig. 7b), whereas peaks of $^{\bullet}OH$ where observed in the corresponding aqueous dispersion (Fig. 7c). The high intensity of both signals is indicative of the important role played by these radical species in the photocatalytic NO oxidation. The four characteristic peaks for the DMPO-$^{\bullet}O_2^-$ adduct were observed in the case of the ZnAl-LDH sample [67]. The presence of Fe^{3+} ions induces changes in the shape, and a sextet peaks appear in the sig-

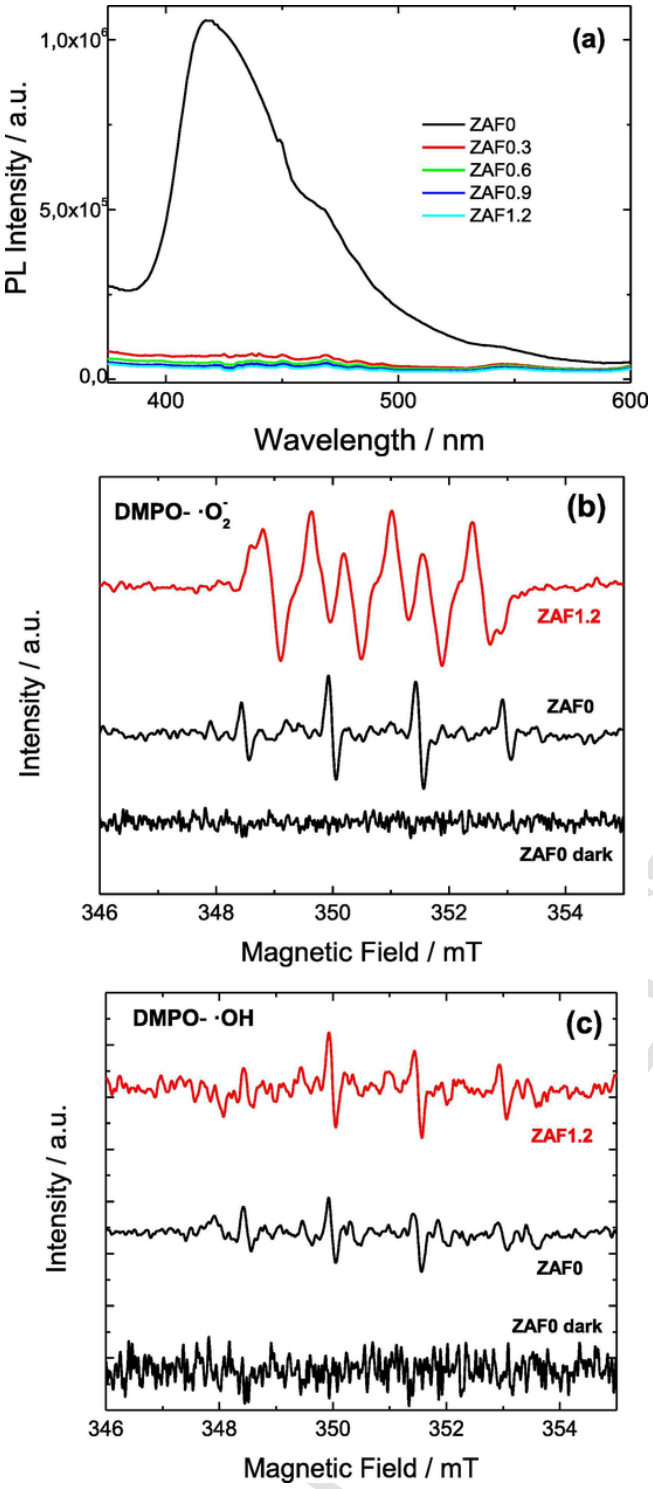

Fig. 7. (a) Photoluminescence (PL) spectra (excitation wavelength = 300 nm) of the different samples. DMPO spin-trapping EPR spectra of the ZAF0 and ZAF1.2 samples under UV–Vis light irradiation for 15 min in (b) methanol solution for $^{\bullet}O_2^-$ and (c) aqueous solution for $^{\bullet}OH$.

nal measured for the ZnAlFe-LDH samples, resembling those observed for Zn-Fe based compounds [68,69]. The intensity of the signal increases with the Fe content (Fig S7). In agreement with the commented MMCT transition mechanism, ZnAlFe-LDH samples displayed much stronger $^{\bullet}O_2^-$ signals indicating that more radicals are produced by Fe substitution. For all the samples, the signal of DMPO-$^{\bullet}$OH adduct was constituted by quartet peaks featuring a 1:2:2:1 intensity ratio. The results commented above confirm the generation of reactive species and their involvement in NO and NO_2 photochemical oxidation, this being enhanced for the ZnAlFe-LDH photocatalyst.

4. Conclusions

ZnAlFe-CO_3 LHDs were studied as UV–Vis light photocatalysts for the photochemical oxidation of NO gas. The LHDs were prepared by the coprecipitation method, the Al^{3+} ion being gradually replaced by Fe^{3+} in the 0.33 to 1.55 Fe/Al ratio range. All the samples crystallized as pure LDH phase except Fe/Al = 1.55. The increased presence of Fe^{3+} ions caused different structural and morphological effects. As the iron content increased, the M^{2+}/M^{3+} ratio and the *c* lattice parameter decreased. Moreover, those samples enriched in iron exhibited the poorest crystallized particles. Consequently, the specific surface area resulted higher for the samples containing iron, and values ranging from 58 to 88 $m^2 \cdot g^{-1}$ were determined for the ZAF0 and ZAF1.2 samples, respectively. Concerning the optical properties, the incorporation of iron ions in the LDH structure resulted in the enhancement of the visible light absorption.

The ZnAlFe-LDH photocatalysts were able to activate the photochemical oxidation of NO molecules under UV–Vis irradiation. The photochemical abatement of NO gas is 4%–11%, increasing with the presence of Fe in the LDH compound. This enhanced photochemical efficiency is related to their higher surface area and the better sunlight harvesting, as the iron centres are responsible for the visible light catalysis. The LDHs samples exhibited ability to adsorb NO_2 gas molecules explaining the outstanding De-NOx selectivity values measured (≈92%), *S* being higher for the iron containing samples. Moreover, the studied photocatalysts are reusable, maintaining good NO removal for an extended period. PL and EPR measurements also served to understand how the electronic properties also assist to the high efficiency found in the removal of NO_X gases. The high radiative recombination rate of the photocharges observed for the non-substituted ZnAl-LDH clearly decreased in iron containing samples, indicating that the presence of the iron centres in the LDH framework must promote a new deactivation pathway for the photocharges. The EPR measurements confirmed the participation of the $^{\bullet}O_2^-$ and $^{\bullet}OH$ reactive species in the photochemical processes involving in the ZnAl-LDH and ZnAlFe-LDH samples. The decay of the PL signal together with the stronger $^{\bullet}O_2^-$ signal observed with the increase of iron content in ZnAlFe-LDH samples suggests a MMCT electron transition through the oxo-bridged M^{III}–O–M^{II} linkages in the LDH framework.

In summary, the Fe^{3+} substitution on the ZnAl-LDH induced changes in the physical and electronic properties producing an enhancement of the accessibility to the reactant molecules, of the light harvesting, of the reaction rates and the availability of the reactive species, all of them increasing the efficiency and selectivity of NO photochemical abatement.

Declaration of Competing Interest

The authors declare that they have no known competing financial interests or personal relationships that could have appeared to influence the work reported in this paper.

Acknowledgements

This work was partly financed by the Junta de Andalucía (PAI Groups FQM-214 and FQM-175) and Spanish Government (MAT2017-88284-P and CTQ2017-84221-R). Rodriguez-Rivas acknowledges a grant from the Fundación Carolina to research at the University of Córdoba (Spain). Adrián Pastor acknowledges a grant from the Ministerio de Educación, Cul-

tura y Deporte (FPU16/05041) to research at the University of Córdoba (Spain).

Appendix A. Supplementary data

Supplementary data to this article can be found online at https://doi.org/10.1016/j.cej.2020.124110.

References

[1] M.C. Newman, W.H. Clements, Ecotoxicology: A Comprehensive Treatment, CRC Press, Boca Raton, Florida, 2008.

[2] B. Yang, K.M. Zhang, W.D. Xu, S. Zhang, S. Batterman, R.W. Baldauf, P. Deshmukh, R. Snow, Y. Wu, Q. Zhang, Z. Li, X. Wu, On-road chemical transformation as an important mechanism of NO_2 formation, Environ. Sci. Technol. 52 (2018) 4574–4582, doi:10.1021/acs.est.7b05648.

[3] R. Zouzelka, J. Rathousky, Photocatalytic abatement of NOx pollutants in the air using commercial functional coating with porous morphology, Appl. Catal. B Environ. 217 (2017) 466–476, doi:10.1016/j.apcatb.2017.06.009.

[4] Y. Chen, J. Borken-Kleefeld, NOx emissions from diesel passenger cars worsen with age, Environ. Sci. Technol. 50 (2016) 3327–3332, doi:10.1021/acs.est.5b04704.

[5] M.W. Frampton, I.A. Greaves, NOx - NOx: who's there?, Am. J. Respir. Crit. Care Med. 179 (2009) 1077–1078, doi:10.1164/rccm.200903-0485ED.

[6] M.L. Williams, D.C. Carslaw, New directions: science and policy – out of step on NOx and NO_2?, Atmos. Environ. 45 (2011) 3911–3912, doi:10.1016/j.atmosenv.2011.04.067.

[7] J. Balbuena, M. Cruz-Yusta, L. Sánchez, Nanomaterials to combat NOx pollution, J. Nanosci. Nanotechnol. 15 (2015) 6373–6385, doi:10.1166/jnn.2015.10871.

[8] H. Chen, C.E. Nanayakkara, V.H. Grassian, Titanium dioxide photocatalysis in atmospheric chemistry, Chem. Rev. 112 (2012) 5919–5948, doi:10.1021/cr3002092.

[9] A. Folli, S.B. Campbell, J.A. Anderson, D.E. MacPhee, Role of TiO_2 surface hydration on NO oxidation photo-activity, J. Photochem. Photobiol. A Chem. 220 (2011) 85–93, doi:10.1016/j.jphotochem.2011.03.017.

[10] G.L. Guerrini, Photocatalytic performances in a city tunnel in Rome: NOx monitoring results, Constr. Build. Mater. 27 (2012) 165–175, doi:10.1016/j.conbuildmat.2011.07.065.

[11] T. Maggos, J.G. Bartzis, M. Liakou, C. Gobin, Photocatalytic degradation of NOx gases using TiO_2 -containing paint: a real scale study, J. Hazard. Mater. 146 (2007) 668–673, doi:10.1016/j.jhazmat.2007.04.079.

[12] R.J. Lewis, N.I. Sax, Sax's Dangerous Properties of Industrial Materials, twelfth, New York, 2012.

[13] J. Ma, H. Wu, Y. Liu, H. He, Photocatalytic removal of NOx over visible light responsive oxygen-deficient TiO_2, J. Phys. Chem. C 118 (2014) 7434–7441, doi:10.1021/jp500116n.

[14] J. Balbuena, M. Cruz-Yusta, A. Pastor, L. Sánchez, α-Fe_2O_3 /SiO_2 composites for the enhanced photocatalytic NO oxidation, J. Alloys Compd. 735 (2017) 1553–1561, doi:10.1016/j.jallcom.2017.11.259.

[15] E.C. Agency, ANNEX 2, Comments and response to comments on CLH proposal on titanium dioxide, 2017. https://echa.europa.eu/documents/10162/4fd87a5d-e671-43e4-a3b8-30e51a723107.

[16] Y. Ye, Z. Zang, T. Zhou, F. Dong, S. Lu, X. Tang, W. Wei, Y. Zhang, Theoretical and experimental investigation of highly photocatalytic performance of CuInZnS nanoporous structure for removing the NO gas, J. Catal. 357 (2018) 100–107, doi:10.1016/j.jcat.2017.11.002.

[17] Q. Zhang, Y. Huang, S. Peng, Y. Zhang, Z. Shen, J. Cao, W. Ho, S.C. Lee, D.Y.H. Pui, Perovskite $LaFeO_3$ -$SrTiO_3$ composite for synergistically enhanced NO removal under visible light excitation, Appl. Catal. B Environ. 204 (2017) 346–357, doi:10.1016/j.apcatb.2016.11.052.

[18] J. Luo, G. Dong, Y. Zhu, Z. Yang, C. Wang, Switching of semiconducting behavior from n-type to p-type induced high photocatalytic NO removal activity in g-C_3N_4, Appl. Catal. B Environ. 214 (2017) 46–56, doi:10.1016/j.apcatb.2017.05.016.

[19] J. Hu, D. Chen, N. Li, Q. Xu, H. Li, J. He, J. Lu, Fabrication of graphitic-C_3N_4 quantum dots/graphene-$InVO_4$ aerogel hybrids with enhanced photocatalytic NO removal under visible-light irradiation, Appl. Catal. B Environ. 236 (2018) 45–52, doi:10.1016/j.apcatb.2018.04.080.

[20] X. Li, W. Zhang, J. Li, G. Jiang, Y. Zhou, S.C. Lee, F. Dong, Transformation pathway and toxic intermediates inhibition of photocatalytic NO removal on designed Bi metal@defective $Bi_2O_2SiO_3$, Appl. Catal. B Environ. 241 (2019) 187–195, doi:10.1016/j.apcatb.2018.09.032.

[21] H. Li, H. Shang, X. Cao, Z. Yang, Z. Ai, L. Zhang, Oxygen vacancies mediated complete visible light NO oxidation via side-on bridging superoxide radicals, Environ. Sci. Technol. 52 (2018) 8659–8665, doi:10.1021/acs.est.8b01849.

[22] H. Wang, Y. Sun, G. Jiang, Y. Zhang, H. Huang, Z. Wu, S.C. Lee, F. Dong, Unraveling the mechanisms of visible light photocatalytic NO purification on earth-abundant insulator-based core-shell heterojunctions, Environ. Sci. Technol. 52 (2018) 1479–1487, doi:10.1021/acs.est.7b05457.

[23] X. Ding, W. Ho, J. Shang, L. Zhang, Self doping promoted photocatalytic removal of no under visible light with bi2moo6: indispensable role of superoxide ions, Appl. Catal. B Environ. 182 (2016) 316–325, doi:10.1016/j.apcatb.2015.09.046.

[24] Y. Gao, Y. Huang, Y. Li, Q. Zhang, J. Cao, W. Ho, S.C. Lee, Plasmonic Bi/$ZnWO_4$ microspheres with improved photocatalytic activity on NO removal under visible light, ACS Sustain. Chem. Eng. 4 (2016) 6912–6920, doi:10.1021/acssuschemeng.6b01852.

[25] R. Sugrañez, J. Balbuena, M. Cruz-yusta, F. Martín, J. Morales, L. Sánchez, Efficient behaviour of hematite towards the photocatalytic degradation of NOx gases, Appl. Catal. B Environ. 165 (2015) 529–536, doi:10.1016/j.apcatb.2014.10.025.

[26] A. Gasparotto, G. Carraro, C. Maccato, C. Sada, J. Balbuena, M. Cruz-Yusta, L. Sánchez, N. Vodišek, U. Lavrencic Štangar, D. Barreca, WO_3 -decorated ZnO nanostructures for light-activated applications, CrystEngComm. 20 (2018) 1282–1290, doi:10.1039/C7CE02148H.

[27] A. Pastor, J. Balbuena, M. Cruz-Yusta, I. Pavlovic, L. Sánchez, ZnO on rice husk: A sustainable photocatalyst for urban air purification, Chem. Eng. J. 368 (2019) 659–667, doi:10.1016/j.cej.2019.03.012.

[28] X. Li, W. Zhang, W. Cui, J. Li, Y. Sun, G. Jiang, H. Huang, Y. Zhang, F. Dong, Reactant activation and photocatalysis mechanisms on Bi-metal@Bi_2GeO_5 with oxygen vacancies: a combined experimental and theoretical investigation, Chem. Eng. J. 370 (2019) 1366–1375, doi:10.1016/j.cej.2019.04.003.

[29] F. Rodriguez-Rivas, A. Pastor, C. Barriga, M. Cruz-Yusta, L. Sánchez, I. Pavlovic, Zn-Al layered double hydroxides as efficient photocatalysts for NOx abatement, Chem. Eng. J. 346 (2018) 151–158, doi:10.1016/j.cej.2018.04.022.

[30] C. Forano, T. Hibino, F. Leroux, C. Taviot-Guého, Layered double hydroxides, in: F. Bergaya, B.K.G. Theng, G.B.T.-D. in C.S. Lagaly (Eds.), Handb. Clay Sci., Elsevier, 2006: pp. 1021–1095. doi:10.1016/S1572-4352(05)01039-1.

[31] M. Shao, J. Han, M. Wei, D.G. Evans, X. Duan, The synthesis of hierarchical Zn-Ti layered double hydroxide for efficient visible-light photocatalysis, Chem. Eng. J. 168 (2011) 519–524, doi:10.1016/j.cej.2011.01.016.

[32] C.G. Silva, Y. Bouizi, V. Fornés, H. García, Layered double hydroxides as highly efficient photocatalysts for visible light oxygen generation from water, J. Am. Chem. Soc. 131 (2009) 13833–13839, doi:10.1021/ja905467v.

[33] N. Ahmed, Y. Shibata, T. Taniguchi, Y. Izumi, Photocatalytic conversion of carbon dioxide into methanol using zinc-copper-M(III) (M = aluminum, gallium) layered double hydroxides, J. Catal. 279 (2011) 123–135, doi:10.1016/j.jcat.2011.01.004.

[34] L. Mohapatra, K. Parida, A review on the recent progress, challenges and perspective of layered double hydroxides as promising photocatalysts, J. Mater. Chem. A. 4 (2016) 10744–10766, doi:10.1039/c6ta01668e.

[35] K.H. Kim, S.K. Pandey, H.T. Nguyen, S.Y. Chung, S.J. Cho, M.Y. Kim, J.M. Oh, Y. Sunwoo, Long-term behavior of particulate matters at urban roadside and background locations in Seoul, Korea, Transp. Res. Part D Transp. Environ. 15 (2008) 168–174, doi:10.1016/j.trd.2009.12.001.

[36] V. Rives, Layered Double Hydroxides: Present and Future, Nova Science Publishers Inc, New York, 2001.

[37] A.V.F. Cavani, F. Trifirò, Hydrotalcite-type anionic clays: preparation, properties and applications, Catal. Today 11 (1991) 173–301.

[38] L. Zheng, N.S. Matin, J. Landon, G.A. Thomas, K. Liu, CO_2 loading-dependent corrosion of carbon steel and formation of corrosion products in anoxic 30 wt.% monoethanolamine-based solutions, Corros. Sci. 102 (2016) 44–54, doi:10.1016/j.corsci.2015.09.015.

[39] J. Winiarski, W. Tylus, K. Winiarska, I. Szczygieł, B. Szczygieł, XPS and FT-IR characterization of selected synthetic corrosion products of zinc expected in neutral environment containing chloride ions, J. Spectrosc. 2018 (2018), doi:10.1155/2018/2079278.

[40] B.R. Strohmeier, W.T. Evans, D.M. Schrall, Preparation and surface characterization of zincated aluminium memory-disc substrates, J. Mater. Sci. 28 (1993) 1563–1572, doi:10.1007/BF00363350.

[41] J. Duchoslav, R. Steinberger, M. Arndt, D. Stifter, XPS study of zinc hydroxide as a potential corrosion product of zinc: rapid X-ray induced conversion into zinc oxide, Corros. Sci. 82 (2014) 356–361, doi:10.1016/j.corsci.2014.01.037.

[42] J.M. García-García, M.E. Pérez-Bernal, R.J. Ruano-Casero, V. Rives, Chromium and yttrium-doped magnesium aluminum oxides prepared from layered double hydroxides, Solid State Sci. 9 (2007) 1115–1125, doi:10.1016/j.solidstatesciences.2007.07.029.

[43] N. Gutmann, B. Müller, Insertion of the dinuclear dihydroxo-bridged Cr(III) aquo complex into the layered double hydroxides of hydrotalcite-type, J. Solid State Chem. 122 (1996) 214–220, doi:10.1006/jssc.1996.0104.

[44] K.S.W. Sing, Reporting physisorption data for gas, solid systems with special reference to the determination of surface area and porosity (Recommendations 1984), Pure Appl. Chem. 57 (1985) 603–619, doi:10.1351/pac198557040603.

[45] D. Carriazo, M. Del Arco, E. García-López, G. Marc, C. Martín, L. Palmisano, V. Rives, Zn, Al hydrotalcites calcined at different temperatures: preparation, characterization and photocatalytic activity in gas-solid regime, J. Mol. Catal. A Chem. 342–343 (2011) 83–90, doi:10.1016/j.molcata.2011.04.015.

[46] K.M. Parida, L. Mohapatra, Carbonate intercalated Zn/Fe layered double hydroxide: a novel photocatalyst for the enhanced photo degradation of azo dyes, Chem. Eng. J. 179 (2012) 131–139, doi:10.1016/j.cej.2011.10.070.

[47] A.A.A. Ahmed, Z.A. Talib, M.Z. Bin Hussein, A. Zakaria, Zn-Al layered double hydroxide prepared at different molar ratios: preparation, characterization, optical and dielectric properties, J. Solid State Chem. 191 (2012) 271–278, doi:10.1016/j.jssc.2012.03.013.

[48] E.M. Seftel, M. Puscasu, M. Mertens, P. Cool, G. Carja, Photo-responsive behavior of γ-Fe_2O_3 NPs embedded into ZnAlFe-LDH matrices and their catalytic efficiency in wastewater remediation, Catal. Today 252 (2015) 7–13, doi:10.1016/j.cattod.2014.11.039.

[49] K. Morimoto, K. Tamura, S. Anraku, T. Sato, M. Suzuki, H. Yamada, Synthesis of Zn-Fe layered double hydroxides via an oxidation process and structural analysis of products, J. Solid State Chem. 228 (2015) 221–225, doi:10.1016/j.jssc.2015.04.045.

[50] A.C. Heredia, M.I. Oliva, B. Agñ, C.I. Zandalazini, S.G. Marchetti, E.R. Herrero, M.E. Crivello, Synthesis, characterization and magnetic behavior of Mg-Fe-Al mixed oxides based on layered double hydroxide, J. Magn. Magn. Mater. 342 (2013) 38–46, doi:10.1016/j.jmmm.2013.04.057.

[51] G. Carja, E. Husanu, C. Gherasim, H. Iovu, Layered double hydroxides reconstructed in $NiSO_4$ aqueous solution as highly efficient photocatalysts for degrad-

ing two industrial dyes, Appl. Catal. B Environ. 107 (2011) 253–259, doi:10.1016/j.apcatb.2011.07.020.
[52] S.M. Xu, T. Pan, Y.B. Dou, H. Yan, S.T. Zhang, F.Y. Ning, W.Y. Shi, M. Wei, Theoretical and experimental study on $M^{II}M^{III}$-layered double hydroxides as efficient photocatalysts toward oxygen evolution from water, J. Phys. Chem. C. 119 (2015) 18823–18834, doi:10.1021/acs.jpcc.5b01819.
[53] S.J. Xia, F.X. Liu, Z.M. Ni, J.L. Xue, P.P. Qian, Layered double hydroxides as efficient photocatalysts for visible-light degradation of Rhodamine B, J. Colloid Interface Sci. 405 (2013) 195–200, doi:10.1016/j.jcis.2013.05.064.
[54] J.Z. Bloh, A. Folli, D.E. Macphee, Photocatalytic NOx abatement: why the selectivity matters, RSC Adv. 4 (2014) 45726–45734, doi:10.1039/c4ra07916g.
[55] S. Öztürk, N. Kilinç, N. Taşaltin, Z.Z. Öztürk, A comparative study on the NO_2 gas sensing properties of ZnO thin films, nanowires and nanorods, Thin Solid Films 520 (2011) 932–938, doi:10.1016/j.tsf.2011.04.177.
[56] J. Balbuena, J.M. Calatayud, M. Cruz-Yusta, P. Pardo, F. Martín, J. Alarcón, L. Sánchez, Mesocrystalline anatase nanoparticles synthesized using a simple hydrothermal approach with enhanced light harvesting for gas-phase reaction, Dalton Trans. 47 (2018) 6590–6597, doi:10.1039/C8DT00721G.
[57] B. Tan, X. Zhang, Y. Li, H. Chen, X. Ye, Y. Wang, J. Ye, Anatase TiO_2 mesocrystals: green synthesis, in situ conversion to porous single crystals, and self-doping Ti^{3+} for enhanced visible light driven photocatalytic removal of NO, Chem. – A Eur. J. 23 (2017) 5478–5487, doi:10.1002/chem.201605294.
[58] J. Liao, W. Cui, J. Li, J. Sheng, H. Wang, X. Dong, P. Chen, G. Jiang, Z. Wang, F. Dong, Nitrogen defect structure and NO+ intermediate promoted photocatalytic NO removal on H_2 treated g-C_3N_4, Chem. Eng. J. 379 (2020), doi:10.1016/j.cej.2019.122282 122282.
[59] M.J. Hernández Rodríguez, E. Pulido Melián, O. González Díaz, J. Araña, M. Macías, A. González Orive, J.M. Doña Rodríguez, Comparison of supported TiO_2 catalysts in the photocatalytic degradation of NOx, J. Mol. Catal. A Chem. 413 (2016) 56–66, doi:10.1016/j.molcata.2015.12.007.
[60] Y. Zhao, X. Jia, G.I.N. Waterhouse, L.Z. Wu, C.H. Tung, D. O'Hare, T. Zhang, Layered double hydroxide nanostructured photocatalysts for renewable energy production, Adv. Energy Mater. 6 (2016) 1–20, doi:10.1002/aenm.201501974.
[61] K. Xu, Z. Zhang, G. Chen, J. Shen, Photoluminescence of colloids of pristine ZnAl layered double hydroxides, RSC Adv. 4 (2014) 19218–19220, doi:10.1039/c4ra01987c.
[62] S.A. Khan, S.B. Khan, A.M. Asiri, Toward the design of Zn-Al and Zn-Cr LDH wrapped in activated carbon for the solar assisted de-coloration of organic dyes, RSC Adv. 6 (2016) 83196–83208, doi:10.1039/c6ra10598j.
[63] N. Baliarsingh, K.M. Parida, G.C. Pradhan, Effects of Co, Ni, Cu, and Zn on photophysical and photocatalytic properties of carbonate intercalated M^{II}/Cr LDHs for enhanced photodegradation of methyl orange, Ind. Eng. Chem. Res. 53 (2014) 3834–3841, doi:10.1021/ie403769b.
[64] K. Parida, L. Mohapatra, N. Baliarsingh, Effect of Co^{2+} substitution in the framework of carbonate intercalated Cu/Cr LDH on structural, electronic, optical, and photocatalytic properties, J. Phys. Chem. C 116 (2012) 22417–22424, doi:10.1021/jp307353f.
[65] N. Baliarsingh, L. Mohapatra, K. Parida, Design and development of a visible light harvesting Ni–Zn/Cr–CO_3^{2-} LDH system for hydrogen evolution, J. Mater. Chem. A 1 (2013) 4236–4243, doi:10.1039/c2ta00933a.
[66] L. Mohapatra, K. Parida, M. Satpathy, Molybdate/tungstate intercalated oxo-bridged Zn/Y LDH for solar light induced photodegradation of organic pollutants, J. Phys. Chem. C 116 (2012) 13063–13070, doi:10.1021/jp300066g.
[67] Y. Cai, H. Song, Z. An, X. Xiang, X. Shu, J. He, The confined space electron transfer in phosphotungstate intercalated ZnAl-LDHs enhances its photocatalytic performance for oxidation/extraction desulfurization of model oil in air, Green Chem. 20 (2018) 5509–5519, doi:10.1039/c8gc02284d.
[68] Y. Huang, D. Zhu, Q. Zhang, Y. Zhang, J. ji Cao, Z. Shen, W. Ho, S.C. Lee, Synthesis of a $Bi_2O_2CO_3/ZnFe_2O_4$ heterojunction with enhanced photocatalytic activity for visible light irradiation-induced NO removal, Appl. Catal. B Environ. 234 (2018) 70–78, doi:10.1016/j.apcatb.2018.04.039.
[69] Q. Yang, S. Wang, F. Chen, K. Luo, J. Sun, C. Gong, F. Yao, X. Wang, J. Wu, X. Li, D. Wang, G. Zeng, Enhanced visible-light-driven photocatalytic removal of refractory pollutants by Zn/Fe mixed metal oxide derived from layered double hydroxide, Catal. Commun. 99 (2017) 15–19, doi:10.1016/j.catcom.2017.05.010.